Advanced Structural Mechanics 2 (2025) 15-28

Advanced Structural Mechanics

Journal homepage: https://asm.sku.ac.ir/

Numerical and Experimental Investigation of Perforation of Flat-ended Fragment Tungsten Heavy Alloy into Thin Metallic Targets

Pouya Pirali[a*], Mostafa Haghighatpour[b]

[a] *Associate professor, Faculty of Materials and Manufacturing Technologies, Malek Ashtar University of Technology, Tehran, Iran.*
[b] *PhD Student in Mechanical Engineering, Faculty of Materials and Manufacturing Technologies, Malek Ashtar University of Technology, Tehran, Iran.*

Article received:2026/01/25, Article revised: 2026/03/17, Article accepted: 2026/03/18

ABSTRACT

Tungsten heavy alloys (WHAs) are high-density materials widely used in ballistic applications because of their superior mechanical strength and high impact resistance. In this study, the perforation behavior of tungsten heavy alloy flat-nosed projectiles with a W90–Ni7–Fe3 composition, manufactured via powder metallurgy, is investigated through combined experimental and numerical approaches. Flat-nosed projectiles with specified dimensions (5.8 mm in diameter and 6.7 mm in length) are launched toward St37 steel targets with thicknesses of 1.5 mm and 3 mm at a controlled impact velocity of 260 m/s. Ballistic experiments are performed using a gas gun system to measure the projectile residual velocity and the maximum back-face deflection (BFD). Experimental results indicate that complete perforation does not occur for the 3 mm thin target, and maximum back-face deflection is 5 mm. In contrast, complete perforation accompanied by plug formation is observed for the 1.5 mm thick target, with residual projectile velocities ranging from 123 to 135 m/s. Numerical simulations of the perforation process are performed using the LS-DYNA finite element code. The Johnson–Cook constitutive and failure models are employed to describe the material behavior of both the projectile and the target. The numerical simulations accurately reproduce the projectile deformation mechanisms and the corresponding failure modes of the target, including plug formation. The numerical simulations show consistent agreement with the experimental observations.

Keywords: Tungsten heavy alloy; Gas Gun; FEM; Metallic target; Perforation; Residual Velocity

* Corresponding author at: Faculty of Materials and Manufacturing Technologies, Malek Ashtar University of Technology, Tehran, Iran
E-mail Address: ppirali@mut.ac.ir
DOI: 10.22034/asm.2026.14892.1024: https://asm.sku.ac.ir/article_116624.html

1. Introduction

Fragment-based warheads represent a typical class of conventional munitions, in which a large number of metallic fragments are generated upon detonation and propelled toward the target with substantial kinetic energy. Among various fragment configurations, prefabricated fragments are widely adopted because their shape and size can be precisely controlled, leading to the improved damage efficiency against specific targets. In such systems, the damage effectiveness is primarily governed by the fragment material, geometry, velocity, and dispersion characteristics. With the continuous improvement of armor protection capabilities, conventional steel fragments often fail to perforate modern target plates, resulting in increasing performance requirements for prefabricated fragments [1-3]. In practical applications, these prefabricated fragments are frequently cylindrical or spherical in shape and deployed in large quantities, forming a dense fragment cloud that impacts structural and armored targets under realistic conditions. Tungsten heavy alloys (WHAs) are two-phase composite materials consisting of spherical tungsten particles embedded in a ductile Ni–Fe matrix. Owing to their high density, excellent mechanical strength, and impact resistance, WHAs are widely used in defense applications such as kinetic energy penetrators and fragmentation warheads. Understanding the perforation behavior and failure mechanisms of WHA projectiles impacting metallic targets is therefore of significant scientific and practical interest [4-6]. Thin metallic targets, including aluminum alloys and low-carbon steels such as St37, are commonly used to investigate the perforation behavior of tungsten-based fragments [7]. Wu [8] conducted a series of experiments to study the failure mechanism of WHA spherical fragments of 2–4 g penetrating into thick armored steel targets at velocities ranging from 500 to 1,300m/s. Ponguru et al. [9] investigated the high-velocity (900-1,400 m/s) penetration of long-rod tungsten alloy projectiles into thick armor steel targets. The failure mechanisms, deformation behavior, crack propagation paths of the projectile and depth of penetration (DOP) were investigated. Feng et al. [10] studied the high-velocity penetration behavior of long rod tungsten alloy projectiles impacting ultra-high-strength steel targets (G50 and 45 steel) at velocities of 689–1489 m/s. Zhang et al. [11] examined the oblique penetration behavior of tungsten spherical fragments with varying diameter (8 and 11 mm) impacting steel plate targets with varying thicknesses (6 and 8 mm). The ballistic limit velocity (V_{50}) was evaluated through experimental testing and numerical simulation. S. Zhao et al. [12] studied the formation and penetration performance of tungsten alloy pre-fragment warheads using static explosion experiments, ballistic gun tests, and numerical simulations. Their results have shown that spherical tungsten pre-fragments impacting steel targets at angles greater than 30° can effectively achieve penetration. Hafizoglu et al. [13] investigated the influence of sintering temperature and Ni/Fe ratio on the ballistic performance of tungsten heavy alloy fragments impacting thick Al 6061-T6 targets at a velocity of approximately 900 m/s, showing that optimized sintering conditions significantly improved residual velocity and perforation performance**.** Chun et al. [14] have developed and validated a finite-element model to investigate the oblique penetration behavior of steel short-rod projectiles (L/D=5) impacting thin metal targets (10mm) at various impact velocities and obliquities. Their results have revealed the dependence of critical ricochet velocity and ultimate penetration velocity on target obliquity, as well as the evolution of projectile velocity, mass, and trajectory during penetration. Cui et al. [15] studied the oblique impact behavior of spherical tungsten alloy projectiles on 12 mm thick 22SiMn2TiB high-strength steel plates at velocities of 500–900 m/s, demonstrating that the ballistic limit velocity increases monotonically with target obliquity. Experimental results have been predicted well by LS-DYNA simulations.

In this study, the perforation response of a short-rod tungsten heavy alloy projectile (L/D < 2) impacting thin low-carbon St37 steel plates with thicknesses of 1.5 mm and 3 mm is investigated at an impact velocity of approximately 260 m/s. Ballistic experiments are conducted to determine the ballistic limit velocity for both target thicknesses, and the associated perforation and failure characteristics are analyzed. The results provide new insight into the perforation mechanisms of tungsten-based fragments under realistic fragment-impact conditions involving moderate velocities and thin metallic targets, which are representative of practical fragmentation warhead applications.

2. Materials and methods

2.1. Material fabrication

Based on the study conducted by Hakan et al. [13], the best perforation performance against multi-layered targets is achieved using a 93W–4.67Ni–2.33Fe tungsten heavy alloy fragment sintered at 1480 °C. The high residual velocity after perforation significantly increases the damage capability of the fragment, enabling it to penetrate and damage a larger number of target layers before completely losing its kinetic energy. Accordingly, in the present study, the specimens are fabricated using the same chemical composition and sintering conditions to ensure consistency and comparability with the reported ballistic performance. Characteristics of powders and Compositions of the samples are shown in Table 1. Powder mixtures are prepared by mixing elemental tungsten, nickel, and iron powders in a turbula mixer at 67 rpm for 45 min. The powder mixtures are pressed in a cold isostatic press under 300 MPa, and then the green samples are sintered at 1480 °C for 20 min under hydrogen (Tdewpoint≤−60 °C) and for 10 min under commercially pure argon in an atmosphere-controlled furnace [13]. The manufactured samples are processed using wire-cut EDM (Electrical Discharge Machining), resulting in cylindrical specimens with dimensions of ϕ5.8 × 6.7 mm. The sintered samples are polished and etched with Murakami's etchant for microstructural characterization via scanning electron microscopy (SEM; 6400 JSM, JEOL. Ltd., Japan). The SEM image of the initial WHA is presented in Fig. 1.

Table 1. Characteristics of Powders and Compositions of Samples [13]

	W	Ni	Fe
Composition (%)	93	4.67	2.33
Particle size FSSS (μm)	4 – 5	4-5	5.2-6.4
Shape	Polygonal	Spherical	Spherical
Purity (wt%)	99.9	99.85	99.5

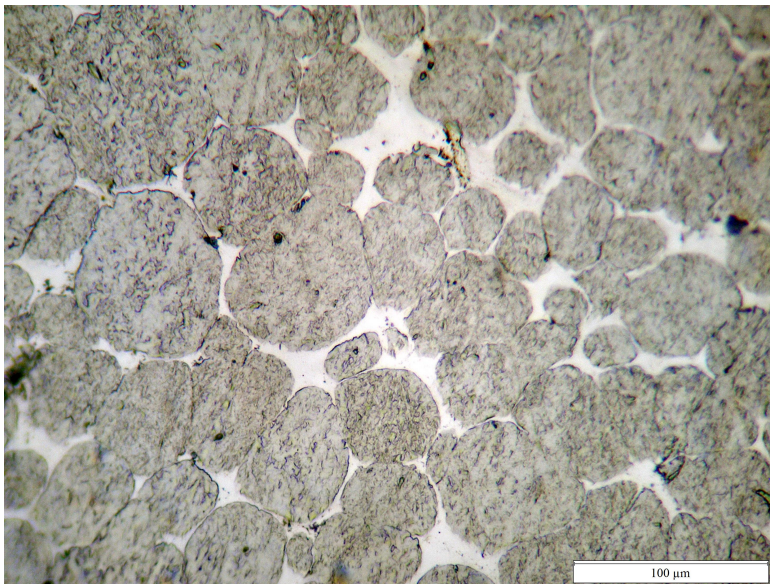

Fig. 1. SEM image of the initial 93W-4.67Ni-2.33Fe heavy alloy, (500×)

The material used in this study is St 37 steel, which is low carbon steel with a carbon content of 0.20% [16]. St37 steel target plates used in the ballistic test with a dimension of 100 mm × 100 mm are machined from larger 1.5 mm and 3 mm by an electrical discharge machining cutting machine.

2.2. Ballistic tests

The ballistic test setup consists of a ballistic gun, sabot baffle, velocity measurement system, target plate, target plate frame, and recovery device placed along the ballistic line, as shown in Fig. 2(d). The impact velocities (Vi) and residual velocities (Vr) of Tungsten are measured. The variable in the tests is the thickness of the target plate. Tungsten heavy alloy fragments are launched from an 8.7-mm-diameter single-stage gas gun to a St37 target. The blunt-nosed cylindrical fragments (5.8 mm in diameter, 6.7 mm in length) shown in Fig. 2 (a), (b), and (c) are placed in a an Ertalon sabot, which assists the acceleration in the barrel. After exiting the barrel, the fragments have 20 cm of free flight before they hit the target. During this flight, pieces of the sabot are separated from the fragments owing to the aerodynamic forces; thus, only the fragments hit the target without obliquity. The velocities of the fragments before and after the perforation of the target are calculated using the velocity measurement system. The dimensions of the deformed fragments and diameters of the holes on the target and back-face deflection (BFD) are measured using a caliper.

2.3. ballistic limit thickness and ballistic limit velocity

For a flat-ended projectile impacting a thin metallic target, the ballistic limit velocity (BLV) is defined as the minimum impact velocity at which complete perforation occurs with zero residual velocity. At this threshold, the projectile's kinetic energy is entirely dissipated through circumferential shear, plastic deformation, and the formation of a disk-shaped plug in the target. When the impact velocity Vi is lower than BLV, only local indentation, plastic deformation, or incomplete plug formation occurs. At Vi=BLV, threshold perforation is achieved, corresponding to the ballistic limit condition. For impact velocities exceeding the BLV, complete perforation takes place and the projectile exits the target with a non-zero residual velocity. The ballistic limit thickness (BLT) is defined as the minimum target thickness that prevents complete perforation for a given impact velocity; when the target thickness equals this critical value, perforation occurs exactly at the threshold condition. In thin targets, the dominant failure mechanism associated with flat-ended projectiles is shear plugging, in which a plug with a diameter approximately equal to that of the projectile is separated from the plate. In other words, when the target thickness is smaller than BLT, complete perforation occurs and the projectile exits the target with a non-zero residual velocity. At the threshold condition (t=BLT), marginal perforation is achieved, characterized by plug separation with zero residual velocity. For target thicknesses greater than BLT, perforation is incomplete and only local indentation or partial shear failure is observed. For flat-ended projectiles impacting thin targets, the ballistic limit thickness increases with increasing shear strength of the target material and decreasing projectile diameter. Typical parameter definitions in BLT and BLVis shown Fig.3.

The perforation behaviour is examined under constant projectile dimensions and impact velocity, with the target thickness considered as the governing variable. The primary objective of this study is to determine the ballistic limit thickness (BLT) corresponding to a specified impact velocity. In this study, the mass, dimension and impact velocity of fragment are 3g, ϕ5.8×6.7 mm, and 260 m/s respectively.

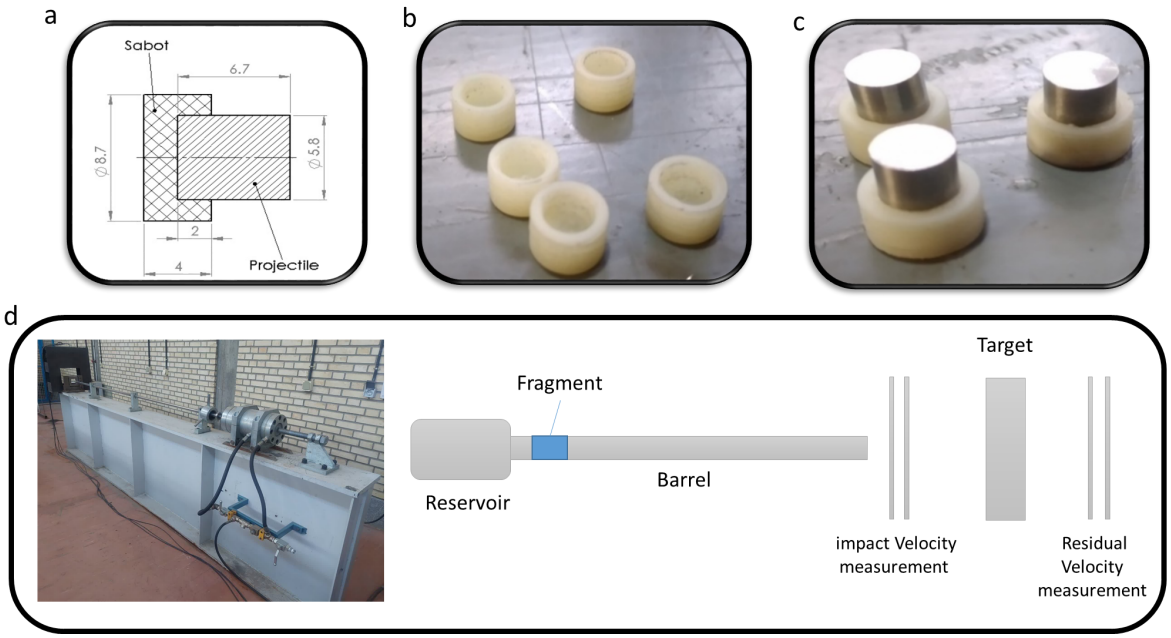

Fig. 2. (a) Dimension of projectile and sabot; (b) sabots; (c) Assembled fragments with the sabot; (d) Schematic view of the ballistic test setup

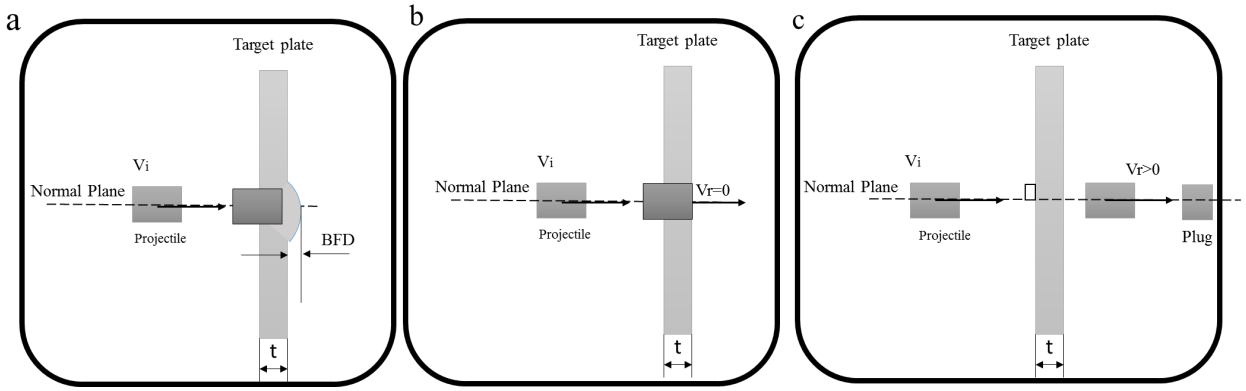

Fig 3. Typical parameter definitions in ballistic limit velocity; (a) Vi<BLV and t<BLT; (b) Vi=BLV and t=BLT; (c) Vi>BLV and t>BLT

2.4. Numerical simulation

Numerical simulations are conducted to analyze the failure mode of WHA flat ended fragments penetrating St37 steel plates. The modeling and meshing work is conducted in Hyper Mesh software, and the model adopts the eight-node hexahedral element. The projectile size and target plate thickness are the same as those in the experiments, and the target plate is a square with a 110 mm length. The sides of the target plate in non-impact direction are set as a single point constraint (SPC) boundary condition. The unit system is cm-g-μs. All of the target plate is encrypted with a grid size of 0.1 mm. The minimum grid size for the tungsten fragment is 0.1 mm. This size generates approximately 2.1 million components in the model. Figure 4 shows the initial finite-element mesh diagram of the fragment and target bodies and local mesh. The erosion contact is set using the Lagrange algorithm. The perforation process of the steel plates impacted by the tungsten fragment is accompanied by high temperature, high pressure, and strain rate effects. The Greisen state equation combined with the JC constitutive model is used to describe the mechanical behavior. The flow stress of Johnson-Cook model can be expressed in the following form [17]:

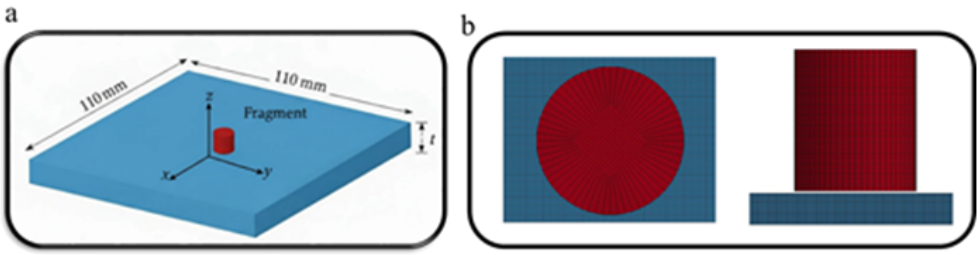

Fig 4. Finite element model; (a) overall Geometry; (b) Local mesh of Fragment and target

$$\sigma = [A + B\varepsilon^{n}][1 + C.\ln \dot{\varepsilon}^{*}][1 - (T^{*})^{m}] \tag{1}$$

$$\dot{\varepsilon}^{*} = \frac{\dot{\varepsilon}_{p}}{\dot{\varepsilon}_{0}} \tag{2}$$

$$T^{*} = \frac{T - T_{ref}}{T_{m} - T_{ref}} \tag{3}$$

Where σ is the flow stress, A, B, n are the strain hardening parameters, C is the strain rate hardening parameter, m is the temperature softening parameter , $\dot{\varepsilon}_0$ is the reference strain rate which is taken to be 0.0000011/s, T_{ref} is the reference temperature, T_m is the melt temperature, and ε is the equivalent plastic stain. The failure of the fragment and the target during the perforation process is modelled using the Johnson–Cook failure model, which is given as [18]:

$$\varepsilon_{f} = [D_{1} + D_{2}\exp(D_{3}\sigma^{*})][1 + D_{4}\ln \dot{\varepsilon}^{*}][1 + D_{5}T^{*}] \tag{4}$$

Where ε_f is the equivalent strain to fracture, σ^* is the ratio of the mean normal stress to the von Mises stress, and D_1, D_2, D_3, D_4, and D_5 are the empirical coefficients of the materials. The damage in any element during the perforation process is calculated using the following equation:

$$D = \sum \frac{\Delta\varepsilon}{\varepsilon_{f}} \tag{5}$$

Where $\Delta\varepsilon$ is the increment in the equivalent plastic strain during an integration cycle. Failure occurs in the element when D equals 1.0. The strength and failure model parameters for the fragment and the target are given in Table 2. The equation of Gruneisen EOS (Equation Of State) can be expressed in the following form:

$$P = \begin{cases} if.\mu \geq 0 \Rightarrow \dfrac{\rho_{0}C^{2}\mu[1 + (1 - \frac{\gamma}{2})\mu - \frac{a^{2}}{2}\mu]}{1 - (S_{1} - 1)\mu - S_{2}\dfrac{\mu^{2}}{\mu + 1} - S_{3}\dfrac{\mu^{3}}{(\mu + 1)^{2}}} \\ if.\mu < 0 \Rightarrow \rho_{0}C^{2}\mu + [\gamma + a\mu]E \end{cases} \tag{6}$$

Where P is pressure, E is relative internal energy, ρ_0 is initial density, C_0 is the intercept of the curve of V_s to V_p, S_1, S_2, and S_3 are the parameters of the curve of V_s to V_p; V_s and V_p are the velocities of shock wave and particles, respectively. M is volume strain, c is Gruneisen constant, a is correction factor which is taken to be zero in this study. The fitting parameters are obtained by combining the stress-strain curves of the St37 at different strain rates and temperatures. The constitutive parameters of the tungsten Fragment material are relatively mature, and the JC material model and JC Failure model parameters of the two materials are listed in Table 2 and Table 3. The Gruneisen state equation parameters are listed in Table 4.

Table 2. JC Material Model Parameters of Target Plate and Tungsten Fragment

Materials	ρ [gr/cm^3]	υ	A [Mbar]	B [Mbar]	C	m	n	Tm [K]	Tr [K]
93W4.67Ni2.33Fe [13]	17	028	0.02	0.00177	0.0195	1.69	0.136	1793	300
St37 Steel [18]	7.85	0.3	0.0035	0.00789	0.022	1	0.83	1811	300

Table 3. JC Failure Model Parameters of Target Plate and Tungsten Fragment

Materials	D1	D2	D3	D4	D5	Cp ($cm^2/\mu s^2.k$)
93W4.67Ni2.33Fe [13]	0	0.33	-3	0.042	0	0.00000132
St37 Steel [18]	0.05	3.44	-2.11	0.002	0.61	0.00000452

Table 4. Gruneisen Equation-of-State Parameters for Tungsten Fragment and Target Plate.

Materials	C (cm/μs)	S1	S2	S3	γ_0	A
93W4.67Ni2.33Fe [19]	0.403	1.237	0	0	1.67	0
St37 Steel [20]	0.459	1.49	0	0	2.17	0.38

3. Results and analysis

3.1. Perforation tests

To investigate the perforation behavior of the projectile, two target thicknesses of 1.5 and 3 mm are considered. Assuming normal impact conditions and an impact velocity of 260 m/s, the corresponding results are presented in Table 5. Perforation process of flat ended fragment into 3 mm thin target is shown in Fig 5. a. According to experimental results, complete perforation is not observed and the Fragment is arrested within the target. This response indicates that the target thickness exceeds the ballistic limit condition for the given impact velocity, resulting in full dissipation of the Fragment's kinetic energy within the plate. Unlike the thinner target, the increased thickness provides sufficient material volume to promote extensive plastic deformation and radial stretching rather than through-thickness shear localization. Upon impact, high compressive stresses are developed beneath the blunt Fragment nose, leading to localized yielding that is followed by progressive plastic flow and bending of the rear surface.

Table 5. Perforation test of Tungsten alloy fragment

No. Shot	t (mm)	Vi (m/s)	Perforation/penetration mode	Vr (m/s)	Max BFD (mm)
1	1.5	260	Full Perforation	130	-
2	1.5	260	Full Perforation	132	-
3	1.5	260	Full Perforation	135	-
4	3	260	No penetration. Stopped in target	-	5
5	3	260	No penetration. Stopped in target	-	5.2
6	3	260	No penetration. Stopped in target	-	5.1

The absence of plug ejection suggests that adiabatic shear band formation does not fully develop across the thickness of the plate, thereby preventing shear-dominated perforation. Instead, energy absorption is governed by a combination of plastic work, membrane stretching, and strain hardening, which collectively reduces the Fragment velocity to zero. The pronounced deformation observed on the back surface further confirms a ductile, non-perforating failure mode, characteristic of thin metallic targets subjected to blunt Fragment impact at velocities below the ballistic limit (similar Fig. 3. a). In this case, the back face deflection (BFD) of the target ranges from 5 to 5.2 mm. Perforation process of flat ended fragment is shown in Fig 5.b. At an impact velocity of 260 m/s, the flat-nosed Fragment fully perforates the 1.5 mm thin steel target, resulting in a residual velocity (Vr) of approximately 130-135 m/s (similar Fig. 3. c). This behavior indicates that the impact velocity significantly exceeds the ballistic limit of the target. The penetration process is dominated by localized plastic deformation and shear failure beneath the Fragment nose, leading to the formation of a well-defined plug. Owing to the blunt geometry of the Fragment, the contact area remains nearly constant during impact, promoting high compressive and shear stresses in the target material rather than progressive penetration. These stresses cause intense plastic flow, followed by adiabatic shear localization around the periphery of the Fragment–target interface. As the shear bands coalesces, a cylindrical plug is separated from the target, which is characteristic of shear-dominated perforation in thin metallic plates. The pronounced permanent deformation observed around the perforation zone further confirms that the target primarily dissipated the Fragment's kinetic energy through plastic work rather than brittle fracture. The relatively high residual velocity suggests limited energy absorption capacity of the thin target, highlighting that thickness plays a critical role in controlling the transition from non-perforation to complete perforation for flat-nosed fragments at moderate impact velocities.

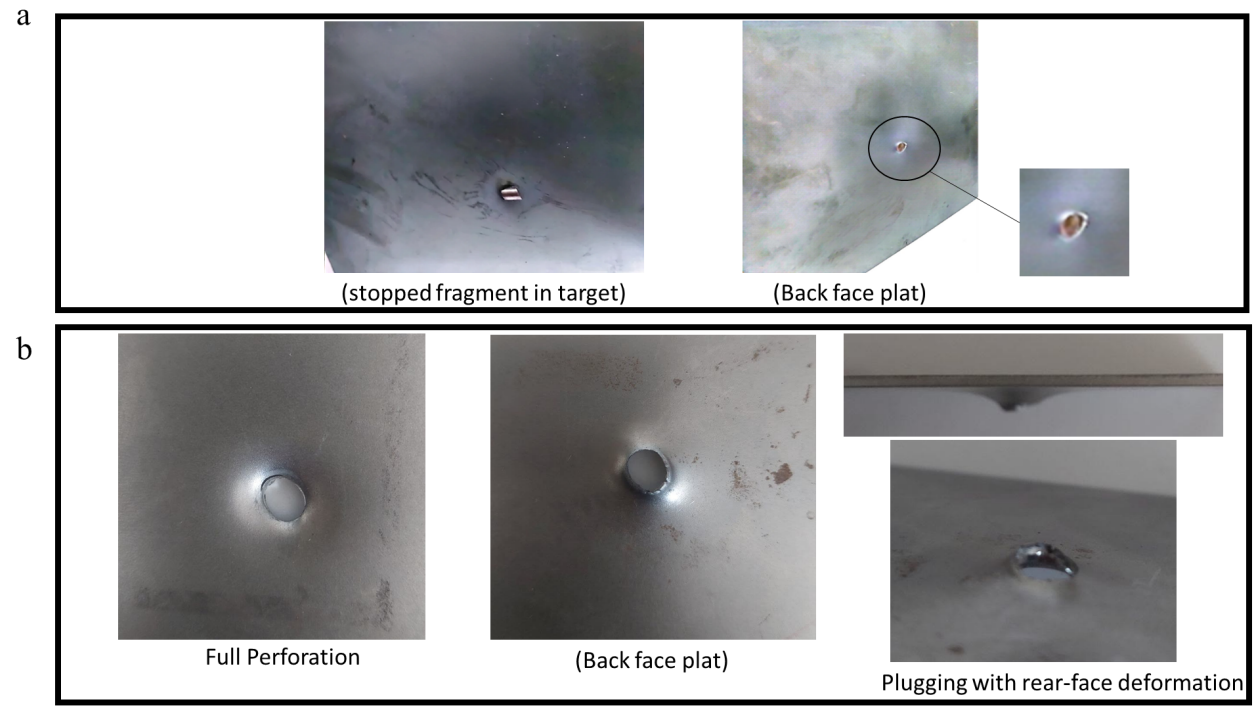

Fig 5. Experimental impact response of steel targets subjected to flat-nosed Fragment impact at 260 m/s; (a) Fragment arrest and large back-face deformation in the 3 mm thick target; (b) Complete perforation of the 1.5 mm thick target

3.2. Simulation results and validation

Simulation results are obtained under different thickness of target conditions by setting a series of simulation constant initial velocity values, and the residual velocity of tungsten alloy fragment perforating a 1.5 and 3 mm thin St37 steel plate is obtained. The residual velocity and BFD and relative errors are listed in Table 6. The average relative error between numerical and experimental residual velocity and BFD is 10 m/s and 7.8%, respectively. Simulation of perforation/penetration of WHA fragment into 1.5 mm thin target is shown in Fig 6.a. For a thin target, complete perforation is observed in the simulation results, accompanied by a significant residual velocity, indicating that the impact velocity exceeds the target's ballistic limit velocity. The dominant failure mechanism in this case is shear plugging combined with localized tensile fracture around the Fragment path, resulting in limited back-face deformation. Due to small thickness, the target is unable to effectively redistribute the impact-induced stresses, and the kinetic energy of the tungsten Fragment is primarily dissipated through localized plastic deformation and material separation. The numerical simulations successfully captured these failure modes and predicted the residual velocity with reasonable agreement, confirming their capability to reproduce the primary penetration mechanisms in thin metallic targets. Figure 7 shows fragment velocity vs. time for this thickness. According results, Residual velocity of fragment is 146 m/s. In contrast, increasing the target thickness to 3 mm fundamentally alters the ballistic response. Simulation of perforation/penetration of WHA fragment into 3 mm thin target shown in Fig 6.b. At this thickness, no complete perforation occurred and the Fragment is fully arrested, demonstrating that the impact velocity is lower than the ballistic limit velocity of the target. Consequently, the 3 mm target can be considered close to or above the ballistic limit thickness for the given impact conditions. In this regime, the penetration process is deformation-controlled rather than perforation-controlled, and the Fragment kinetic energy is mainly absorbed through extensive plastic deformation and bending of the target plate. This behavior is reflected by the pronounced back-face deformation measured experimentally and predicted numerically. Figure 8 shows curve of BFD vs time for this thickness. According to the results, max BFD of target is 5.5 mm. The comparison between simulations and experiments shows good agreement in capturing the overall deformation trend, highlighting the sensitivity of back-face deformation to material damage evolution and stress redistribution. Overall, the results demonstrate a clear transition from complete perforation to energy-absorbing deformation with increasing target thickness, emphasizing the critical role of ballistic limit velocity and thickness in the design and assessment of protective structures. The discrepancies between the experimental and numerical results mainly arise from simplifications in material constitutive and damage models under high strain-rate impact conditions, where localized shear failure, thermal softening, and progressive fracture are difficult to capture accurately. Additional differences stem from numerical idealizations such as perfect geometry, symmetry, and boundary conditions, as well as mesh dependency near the ballistic limit. Experimentally, small variations in impact velocity, Fragment alignment, and measurement of residual velocity and back-face deformation introduce scatter in the data. Material inhomogeneity, thickness tolerances, and microstructural defects further affect the penetration response. Overall, the observed level of error is consistent with the reported ballistic impact studies and does not compromise the validity of the numerical model in predicting the dominant failure mechanisms.

Table 6. Comparison of Residual Velocity and BFD between Simulation and Test Results.

No. Shot	t (mm)	Vi (m/s)	Vr (m/s)			BFD (mm)		
			Test	Simulation	Error (%)	Test	Simulation	Error (%)
1	1.5	260	130		12	-	-	-
2	1.5	260	132	146	10	-	-	-
3	1.5	260	135		8	-	-	-
4	3	260	-	-	-	5		10
5	3	260	-	-	-	5.2	5.5	5.7
6	3	260	-	-	-	5.1		7.8

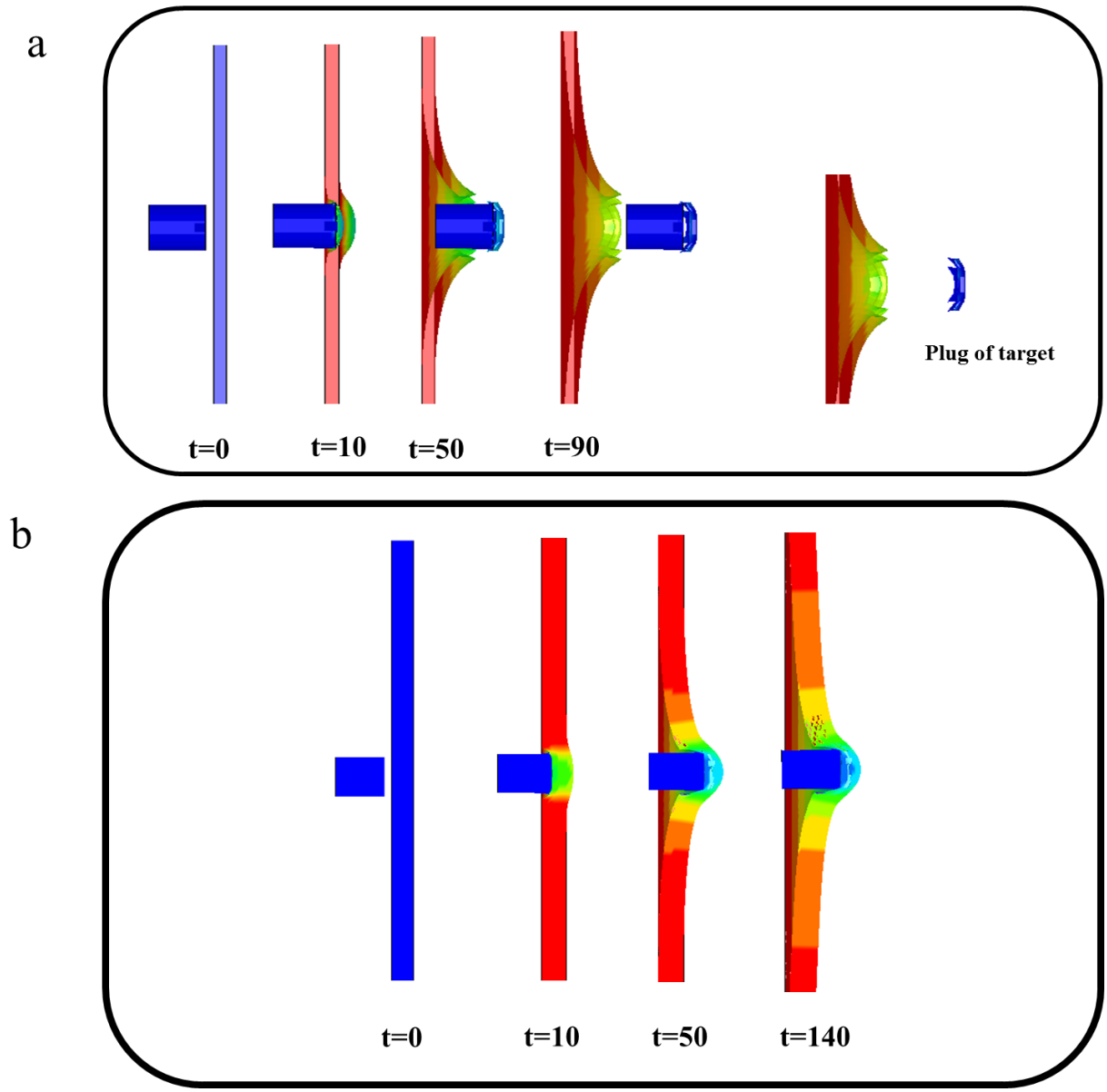

Fig 6. Simulation of WHA Fragment penetration into target; (a) Thickness 1.5 mm; (b) Thickness 3 mm

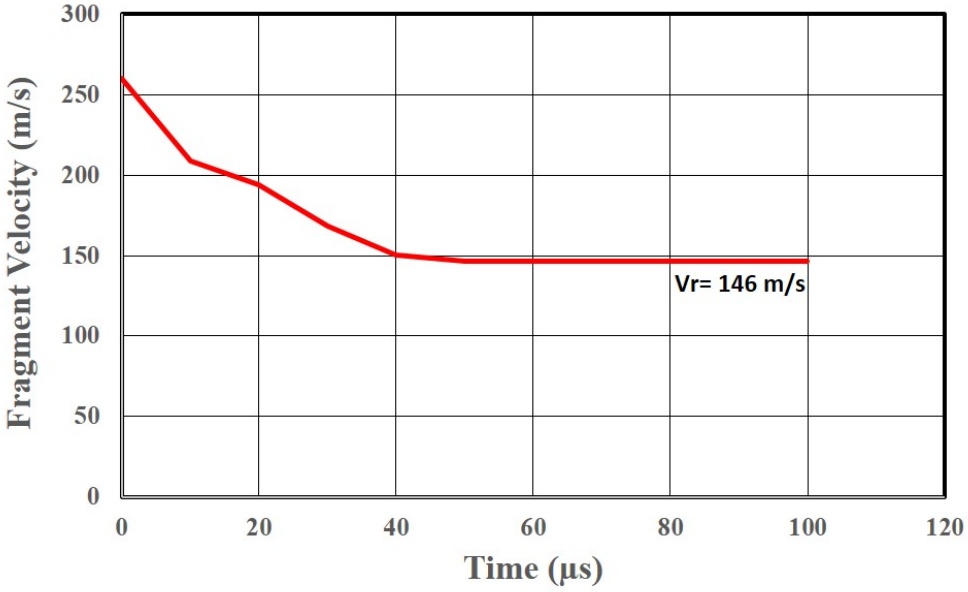

Fig. 7. Fragment Velocity vs. Time for 1.5 mm Target Thickness and V_i = 260 m/s.

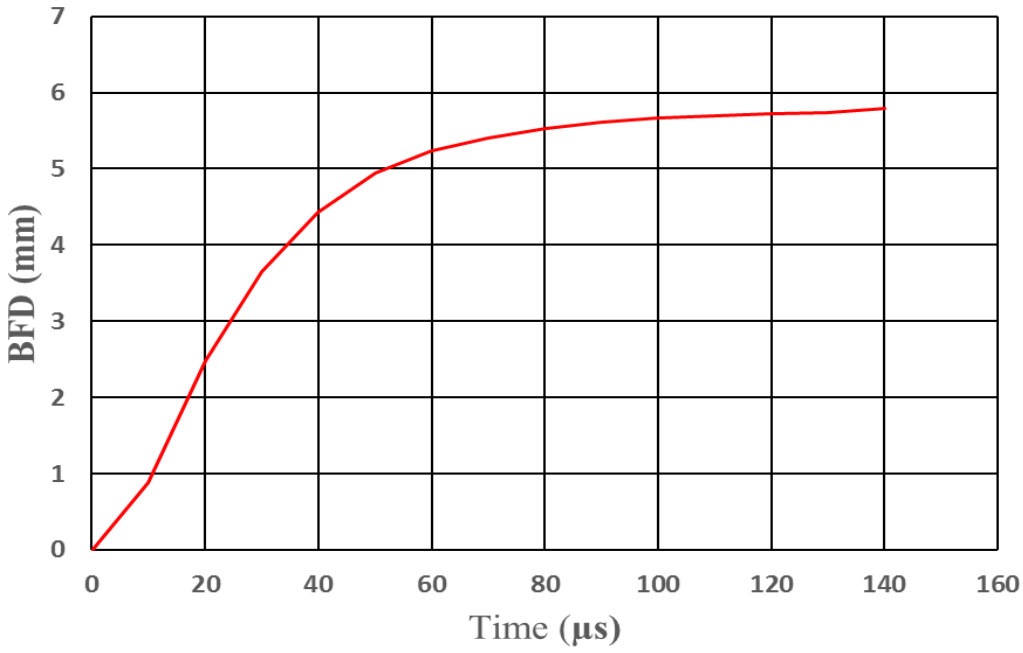

Fig 8. BFD vs. Time for 3 mm Target Thickness and Vi=260 m/s.

3.3. Determination of the Ballistic Limit Velocity and Ballistic Limit Thickness

The numerical results demonstrate a clear transition in the penetration behavior with increasing impact velocity. Table 7 presents the numerical simulation results of WHA fragment penetration/perforation into a 1.5 mm thin St37 steel target. At impact velocities of 215 and 245 m/s, the Fragment is fully arrested by the target and no residual velocity is observed, indicating that the impact velocity is below the ballistic limit and complete perforation does not occur. When the impact velocity increases to 250 m/s, a non-zero residual velocity is recorded, marking the onset of complete perforation and suggesting that the ballistic limit velocity lies between 245 and 250 m/s. Ballistic limit velocity in thickness is 247 m/s. Further increases in impact velocity lead to a rapid rise in residual velocity, from 87 m/s at 250 m/s to 146 m/s at 260 m/s, reflecting reduced energy absorption by the target once perforation is achieved. At the highest simulated impact velocity of 350 m/s, the residual velocity reaches 280 m/s, indicating a perforation-dominated regime where the target offers limited resistance, and energy dissipation is primarily localized near the penetration zone. Overall, the results highlight the strong dependence of penetration response on impact velocity and enable a reliable estimation of the ballistic limit velocity based on the transition from zero to non-zero residual velocity. In order to determine the ballistic limit thickness, numerical simulations are performed for a tungsten fragment at a constant impact velocity of 260 m/s for different target thicknesses, and the corresponding results are presented in Table 8. Numerical results show that for a 1.5 mm St37 steel plate, the ballistic limit velocity is approximately 247 m/s. At an impact velocity of 260 m/s, this thickness is below the ballistic limit, resulting in the complete perforation with a residual velocity. By increasing the target thickness, the ballistic limit velocity increases, and the Fragment is fully stopped at a thickness of 2.2 mm. Accordingly, the ballistic limit thickness corresponding to an impact velocity of 260 m/s is determined to be 2.2 mm.

Table 7. Numerical Simulation Results for Various Impact Velocities on a 1.5 mm Thin St37 Steel Target.

No.	t (mm)	Vi (m/s)	Vr (m/s)	Numerical observations
1	1.5	215	0	No Perforation
2	1.5	245	0	No Perforation
3	1.5	247	0	Full perforation with the residual velocity equal to zero (BLV)
4	1.5	250	87	Full perforation
5	1.5	255	119	Full perforation
6	1.5	260	146	Full perforation

Table 8. Numerical Simulation Results for Various Target Thicknesses Impacted by a WHA Fragment at 260 m/s.

No.	Vi (m/s)	t (mm)	Vr (m/s)	Numerical observations
1	260	1.5	146	Full perforation with the residual velocity
2	260	2.1	32	Full perforation with the residual velocity
3	260	2.2	0	Full perforation with the residual velocity equal to zero (BLV)
2	260	2.4	0	No Perforation
3	260	3	0	No perforation

4. Conclusion

A comprehensive numerical investigation is carried out to examine the ballistic performance of St37 steel targets under normal impact conditions using the LS-DYNA finite element code in conjunction with the Johnson–Cook constitutive and failure models and the Grüneisen equation of state. The simulation results successfully reproduce the key physical characteristics observed in ballistic impact tests, demonstrating high fidelity in predicting both penetration and residual velocity. For the 1.5 mm thick plate, the numerical model identifies a ballistic limit velocity of approximately 247 m/s, at which complete perforation occurs with zero residual velocity. Increasing the impact velocity to the range of 250–260 m/s leads to full perforation with progressively larger residual velocities, which is consistent with experimental trends. By evaluating thicker targets, the ballistic limit thickness for the selected impact velocity of 260 m/s is determined to be 2.2 mm, representing the critical thickness required to fully arrest the fragment. Validation against experimental data confirms that the proposed numerical model accurately captures the transition from partial to full perforation, with an average deviation of about 10–12 %, which is acceptable for high-strain-rate impact simulations. This agreement demonstrates the reliability of the numerical framework for predicting ballistic limits and penetration mechanisms under various loading conditions. In summary, the proposed approach provides both a quantitative and mechanistic understanding of the ballistic resistance of structural steel targets. The established correlation between impact velocity, plate thickness, and residual velocity offers a valuable basis for optimizing lightweight protective structures and guiding future experimental and computational studies on metallic target perforation.

References

[1] Baek, J., Lee, S.P., Lee, Y.J., Kim, S.U., 2018. Design of Subminiaturized Natural Fragment Warhead based on the Analysis of Warhead Effectiveness. Journal of the Korean Society for Precision Engineering. 35, 933-941.

[2] Zhao, J., Fu, J.P., Chen, Z.G., Guo, Z.Y., Zhang, J., Zheng, C.J., 2019. Analysis of Forming and Spreading of Pre-Formed Fragment Warhead. Journal of Ordnance Equipment Engineering. 40, 62-66.

[3] Mei, R.B., Feng, T.Y., Huang, B., Zhang, H.J., Li, M.Y., Zhang, B.H., 2022. Numerical simulation and structural optimization of cylindrical prefabricated fragments under explosion impact. Journal of Plasticity Engineering. 29, 197-203.

[4] Durlu, N., Caliskan, NK., Bor, S., 2014. Effect of swaging on microstructure and tensile properties of W–Ni–Fe alloys. Int J Refract Met Hard Mater. 42, 126–131.

[5] Zhang, J., Xu, Y.X., Liu, T.L., Zhang, P., 2022. Oblique Penetration effect of a Tungsten Ball on High Hardness Steel. Explosion and Shock Waves. 42, 71-82.

[6] Ma, Y., He, Y., Wang, C.T., He, Y., Guo, L., 2022. Response behavior of double layer tungsten fragments under detonation loading. Journal of North western Polytechnical University. 40, 819-828.

[7]Borvik, T., Hopperstad, O.S., Berstad, T., Langseth, M., 2002. Perforation of thin steel plates by blunt and ogival projectiles. International Journal of Impact Engineering. 27, 19–35.

[8] Wu, X., 1999. Research on penetration theory and experiment of tungsten alloy spherical fragment against finite thickness target. PhD Thesis, Chinese. Beijing: Beijing institute of technology.

[9] Ponguru, S.P., Rama Subba, R.P., Sreekantha R. T., 2019. Scaled WHA long rod projectile impact against an armour steel. Human Fact. Mech. Eng. Def. Safe. 13, 33–39.

[10] Feng, X.W., Li, J., Lu, Y., Wang, S., Lu, Z., Liu, C., Fu, Dan., 2023. Characteristics of high-mass tungsten alloy kinetic projectile penetrating ultra-high strength steel targets at high velocity. EXPLOSION AND SHOCK WAVES. 43, No. 9.

[11] ZHANG, Jian., XU, Y., LIU, T., ZHANG, P., 2022. Oblique penetration effect of a tungsten ball on high hardness steel. EXPLOSION AND SHOCK WAVES. 42, No. 2.

[12] Zhao, S., Yuan, S., Cheng, C., Shi, X.S., Fu, Y., Wang, Y.C., 2023. Simulation on forming and penetrating target plate of tungsten alloy pre-fragment warhead. Int. Jnl. of Multiphysics. 17, 2.

[13] Hakan, H., Nuri, D., Emrah K.H., 2019. Effects of sintering temperature and Ni/Fe ratio on ballistic performance of tungsten heavy alloy fragments. International Journal of Refractory Metals & Hard Materials. 81,155–166.

[14] Chun, C., Yingqian, F.u., Chengxin, D.u., Guang, Li., Shuang, Z., Zhonghua, D.u., Kun, Z., Feng, Z., Zhaoxiu, J., 2024. Oblique penetration law of short-rod projectile into thin metal target. Mechanics of Advanced Materials and Structures. 31,9.

[15] Cui, X.Y., Hao, X., Han, H.Y., Tao, W., Huang, G.y,.2024. Oblique penetration of spherical tungsten alloy projectiles on high-strength steel plates. International Journal of Impact Engineering 192, 105030.

[16] Saber, M., Balhassn, A., 2021. On the Determination of Material Mechanical Properties of St 37 Steel Pipes Using O-Ring Specimens. Experimental Techniques.

[17] Johnson, G.R., Cook, W.H., 1983.A constitutive model and data for metals subjected to large strains, high strain rates and high temperatures. Proceedings of the 7th International Symposium on Ballistics. 21, 541–547.

[18] Mohammadi Hooyeh, H., Naddaf Oskouei, A., Mirzababaie Mostofi, T., Vahedi, Kh., 2023. Investigation of Oblique Blast Loading on Trapezoidal Corrugated Core Sandwich Panels; Experimental and Numerical Study. Journal of Solid Mechanics 15, 1, 109-119.

[19] M. K. Mohd nor, M.K., Ho, C.S., Maat, N., Kamarulzaman, M.F., 2019. Modelling shock waves in composite materials using generalised orthotropic pressure. Continuum Mech. Thermodyn.

[20] Bataev, I.A., Tanaka, S., Zhou, Q., Lazurenko, D.V., Jorge Junior, A.M., Bataev, A.A., Hokamoto, H., Mori, A., Chen, P., 2019. Towards better understanding of explosive welding by combination of numerical simulation and experimental study. Materials & Design, 169, 107649.